GeoScienceWorld
Lithosphere
Volume 2022, Article ID 9074201, 13 pages
https://doi.org/10.2113/2022/9074201

Lithosphere

Research Article

A Millennial-Scale Tephra Event-Stratigraphic Record of the South China Sea since the Penultimate Interglacial

Weijia Feng,[1] Jiawen Yang,[1] Chuang Bao,[1] Deming Kong,[1,2,3] and Min-Te Chen[4]

[1]*Laboratory for Coastal Ocean Variation and Disaster Prediction, College of Ocean and Meteorology, Guangdong Ocean University, Zhanjiang, Guangdong 524088, China*
[2]*Key Laboratory of Climate, Resources and Environment in Continental Shelf Sea and Deep Sea of Department of Education of Guangdong Province, Guangdong Ocean University, Zhanjiang, Guangdong 524088, China*
[3]*Shenzhen Research Institute of Guangdong Ocean University, Shenzhen 518108, China*
[4]*Institute of Earth Sciences, Center of Excellence for the Oceans and Center of Excellence for Ocean Engineering, National Taiwan Ocean University, Keelung 202, Taiwan*

Correspondence should be addressed to Deming Kong; kongdm@gdou.edu.cn and Min-Te Chen; whoimtchen@gmail.com

Received 30 April 2022; Revised 18 October 2022; Accepted 12 November 2022; Published 28 November 2022

Academic Editor: Jean Borgomano

Large volcanic eruptions have significant impacts on climate and environmental changes. The deposition of tephra in marine sediments may serve as an eruption recorder, but it has not been extensively studied in the western Pacific. This study explored a millennial-scale tephra event-stratigraphy with multiple indicators in a sediment core collected from the eastern South China Sea (SCS) basin. The magnetic susceptibility (MS), Fe and Mn concentrations determined by X-ray fluorescence (XRF), and identification of individual ash particles were used to identify tephra layers and reconstruct the history of volcanic activity. Nine visible volcaniclastic units (VVU) and two cryptotephra layers have been identified based on their distinct features, as manifested by high MS, Fe, and Mn concentrations and single-peak grain size distribution. The VVUs and cryptotephra layers reveal elevated volcanic activities. Using the radiocarbon age model and oxygen isotope stratigraphy, these episodes could roughly correspond to the following periods: 1-11 ka, 16-17 ka, 27-31 ka, 41-42 ka, 45-46 ka, 49-50 ka, 77-80 ka, 90-91 ka, 97-99 ka, 116-126 ka, and 132-140 ka. The alkenone-derived SST has significant glacial cycles and good synchronicity with other SCS SST records, which could partially help build the preliminary age model. Despite possible age errors larger than 1 kyr, the discovery and timing of tephra layers provide a preliminary framework to further investigate the impact of historical volcanic eruptions on climate changes.

1. Introduction

Large volcanic eruptions significantly impact the climate and regional environment due to the release of large amounts of tephra and aerosols into the atmosphere and earth's surface [1–3]. In particular, volcanic aerosols significantly reduce the solar radiation to the earth's surface, leading to regional or even global climatic perturbations [2, 4]. It would have wide-ranging impacts on human society. For example, a submarine volcano in Tonga recently erupted on 15 January 2022, blasted voluminous ashes to over 55 km in height and hundreds of miles away, and triggered a tsunami and great destruction in the South Pacific. The South China Sea (SCS), one of the largest marginal seas in the western Pacific, is surrounded by two active volcanic island arcs (the Philippine and Sunda arcs). The explosive eruption of Mount Pinatubo in 1991 ejected 20 million tons of SO_2 into the stratosphere and more than 5 km^3 of material into the air [5, 6]. It caused earthquakes, extreme climate, and significant economic losses worldwide. Volcanic eruptions in this region were found increased ENSO activity and led to chain effects on regional and global climate changes [7]. Therefore, large volcanic eruptions (Volcanic Explosivity Index (VEI) $> 6+$) are rare opportunities for scientists to examine the response of climate and environment to such extreme events. However, large eruptions like the Pinatubo do not

frequently occur on centennial or millennium scales. So, it is necessary to find more volcanic eruption records from tephra deposits, which are usually preserved in lacustrine or marine sediments [8–11]. Accordingly, 213 tephra layers have been identified from 56 marine sediment cores and linked to land volcanic eruptions in Mesoamerica [12]. The tephra records and their volcanic chronological signatures from the Izu-Bonin arc have also been used to trace their sources [13].

In the SCS, the volcanic ash layers were identified by visual inspections in the marine sediment core MD972142 [14–17] (Figure 1). However, some tephra layers might be too thin to be visible, as the core site is quite far from the volcanic craters. Additionally, the tephra sinking processes might also be influenced by meteorological and oceanic factors such as currents, resuspension, or bioturbation in sediment particles [18], which could make the tephra layer hard to be identified. To better acquire tephra event-stratigraphy, continuous marine sediments with sensitive tephra chemical or physical indicators are essential to identify the volcanic eruption events. Here, we report a sediment core KK2002-K3 collected from the eastern SCS basin (Figure 1) near the Philippines and used multiple indicators such as magnetic susceptibility, grain size, color spectrophotometry, $U^{K'}_{37}$-SST record, and element concentrations determined by X-ray fluorescence (XRF) to build the tephra event-stratigraphy (Figure 1).

2. Study Area and Core Sampling

The SCS is located between the Eurasian and Pacific plates, surrounded by the Philippine and Sunda arcs. The surface sediments in the eastern SCS basin are mainly composed of montmorillonite derived from the chemical weathering of andesitic-basaltic rocks in Luzon Island [19]. Two types of tephra sediments have been distinguished: one with colorless glass-hornblende assemblages belonging to an acidic volcaniclastic layer and the other volcaniclastic layer with an assemblage of less volcanic glass and brown glass-augite-magnetite deposits [14].

The source of tephra in the eastern SCS is mainly the Ryukyu-Taiwan-Philippine volcanic arc and the Sunda volcanic arc, which have more than 750 active or potentially active volcanoes (Figure 1) [20]. According to the Smithsonian Institution's Global Volcanism Program (GVP; https://volcano.si.edu/) and the Large Magnitude Explosive Volcanic Eruptions (LaMEVE) database of the Volcanic Global Risk Identification and Analysis Project (VOGRIPA) [21], three volcanoes with eruptive index (VEI) > 6 (global impact) have erupted in the Philippines since 1.2 Ma. The most recent eruption of Pinatubo was in 1991. The ash covered about 30% area of the SCS, and tephra thickness in the sediment could reach up to 45 mm [17]. The physical characteristics and chemical composition of tephra layers significantly differ from those of the common deep-sea sediments [22, 23], such as colors, magnetism, and major elements.

The content of the volcanic glass is especially high in tephra layers, and the volcanic glass is amorphous and completely extinct. Usually, acid volcanic glass is colorless

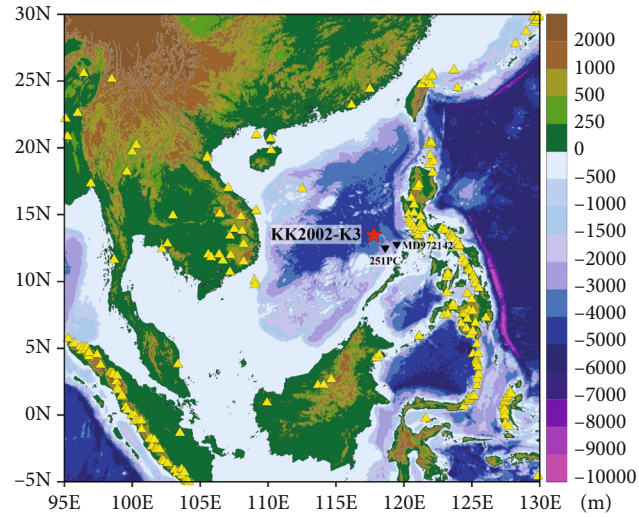

Figure 1: Locations of site KK2002-K3 and the referenced sites (251 PC [40] and MD972142 [15]). Yellow triangles indicate Pleistocene and Holocene active volcanoes (GVP) [21].

and transparent, while basaltic volcanic glass is transparent or nearly transparent brown-green or yellow-brown. The morphological characteristics of volcanic glass are very important bases for identification under the microscope. Under the microscope, the surface of volcanic glass is flat or curved, and many have air bubbles. If the bubble is complete, it will be a round or elongated thin tube. Otherwise, the edge will be sharp and broken, with commonly curved arcs and sharp corners.

The sediment core KK2002-K3 (13.5190°N, 117.7788°E, water depth 3947 m) was collected onboard R/V "Tan Kah Kee" by a gravity corer in the eastern basin of SCS in June 2020. The core is 3.6 m in length, cut into three sections, and kept in a freezer at 4°C on board. Then, the cores were carried to the Guangzhou Marine Geological Survey for core logging.

3. Analytical Methods

3.1. Core Logging. The cores K3 were logged in the Guangzhou Marine Geological Survey in August 2020. The cores were cut into two halves with a core cutter, with one for archive and the other one for study. The surface of the studied core was flattened and scraped with a clean plastic sheet for core logging. The logging was completed by a multisensor core logger system (MSCL of company GeoTek™) at 5 mm intervals [24, 25]. The magnetic susceptibility (MS) was measured by a Bartington MS2E point sensor [24]. Using MS to analyze sediment cores is a common, nondestructive, and fast method to detect tephra layers [12, 26–28]. MS can be readily identified in Mg-Fe-rich tephra layers. But the identification of cryptotephra has been more challenging [29–31]. The Bartington MS2E point source sensor integrates MS measurements over 3.8 mm [32] and is suitable for detecting small, discrete sediments (area of response: 3.8 mm*10.5 mm). The MS2E is particularly

suitable for identifying tephra and cryptotephra together with other tephra-indicative parameters [25].

The elemental concentration was measured by an XRF sensor (Olympus VANTA-C). We used a rhodium (Rh) anode target ray tube with a voltage of 40 kV and a time of 10 s per spot. To improve the signal-to-noise ratio, the surface of sediments was flattened carefully to minimize the influence of surface roughness. The results were given as element concentration in unit ppm with calibration by standard sample. Repeated scanning results show that their differences are less than 10% SD, suggesting that the XRF results are repeatable. Although many high-resolution stratigraphic and paleoclimatic studies are based on XRF results [28, 33, 34], if the cores were not dried for logging, sediment moisture might influence the elemental concentration results. So, the XRF element concentrations might not be accurate and were thus used to semiquantitatively reveal significant changes in this study. Meanwhile, elemental units were converted from ppm to percentage (%).

The MSCL logger was equipped with a Konica Minolta color spectrophotometer that measures the surface reflectance in 10 nm spectral bands at 0.5 cm intervals, from near UV wavelengths to very near IR wavelengths (approximately 360-740 nm). Color spectrophotometry is a nondestructive technique that can produce reflectance data at 3 mm resolution. In turn, the resulting data can be used to record the sediment's optical properties, with L^* and grayscale representing brightness and reflectance gradients (0 for black and 100 for pure white, respectively). The actual color (hue) is represented by the letters a^* (negative values are red; positive values are green) and b^* (negative values are blue; positive values are yellow) [35]. Light reflectance and luminescence were used as indicative properties of tephra shards preserved. Several studies have used this methodology and other indicators to identify tephra layers [31, 36]. However, it has been noted that low concentrations of shards and highly dissimilated tephra layers may not be discernible from the nonvolcanogenic sediments [18].

3.2. Radiocarbon and Oxygen Isotope Analysis. The logged cores were subsampled at 3 mm intervals with special equipment invented by the authors (patent No. ZL202022414864.1). The subsampling equipment consists of 12 semicircles 0.2 mm thick stainless steel plates, interluded by 3 mm thick Teflon plates to keep subsampling intervals fixed. Each sample slice is in a good semicircle shape and can be observed for sediment properties and fossils. Four subsamples were picked for foraminifera for radiocarbon dating. The planktonic foraminifera shells of *Globigerinoides ruber* and *Globigerinoides sacculifer* were handpicked under a microscope and then cleaned with MilliQ water in ultrasonic. About 5-8 mg of foraminifera shells for each sample was sent to the State Key Laboratory of Isotope Geochemistry of Guangzhou Institute of Geochemistry (GIG) for further pretreatment and graphitization. Then, the accelerator mass spectrometry (AMS) ^{14}C measurements were performed in the AMS lab in the State Key Laboratory of Organic Geochemistry, GIG Chinese Academy of Sciences. The AMS ^{14}C ages were calibrated

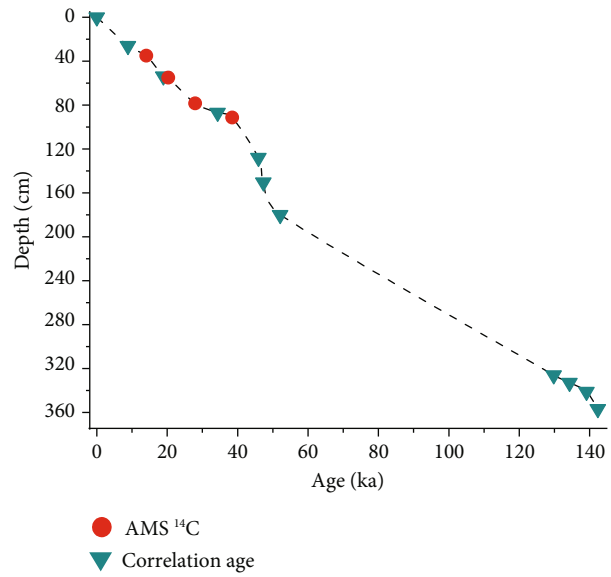

Figure 2: Age-depth model of core KK2002-K3 combining accelerator mass spectrometry (AMS) ^{14}C data and correlation ages. The red circles indicate the AMS ^{14}C age, the green inverted triangles indicate the correlation age, and dotted lines between adjacent age data show the linear interpolations.

using the software Calib 8.10 and the database Marine 20 with the setting $\triangle R = 0$ (Figure 2).

As the ^{14}C age at 91 cm almost reaches the limits of radiocarbon dating, stable oxygen isotope of planktonic foraminifera *Globigerinoides ruber* (white species with grain size larger than 74 μm) was also measured to help build an age model. A total of 58 samples of *G. ruber* were picked up, rinsed ten times with deionized water, and then dried in an oven at 60°C. The samples were analyzed by stable isotope ratio mass spectrometry (Thermo Delta V Advantage) with an automated carbonate preparation system (Gasbench II). To extract the carbonate fractions from powdered samples, the foraminifera shells were treated with dehydrated phosphoric acid at 70°C for 60 min under vacuum. The isotopic ratios are expressed in δ notation as per mil (‰) deviation relative to the VPDB standard. The experiments were conducted at the Key Laboratory of Guangdong Higher Education Institute of Climate, Resources and Environment on the Shelf and Deep Sea, Guangdong Ocean University. Analytical precisions for $\delta^{13}C$ and $\delta^{18}O$ were less than 0.2‰. Few or no foraminiferal shells were found between the core depths of 192-323 cm.

3.3. Grain Size Analysis. About 0.5 g of dry sediments was pretreated for grain size analysis. Organic matter and carbonate in the bulk samples were carefully removed using 10% H_2O_2 (24 h) and 10% HCl (24 h) in a water bath at 60°C. Afterward, approximately 10 ml of a dispersant sodium hexametaphosphate $[(NaPO_3)_6]$ solution was added and pretreated with ultrasonic pretreatment for 15 min to disperse the particles. For each sample, grain size distribution was measured with a Malvern Mastersizer 3000 laser

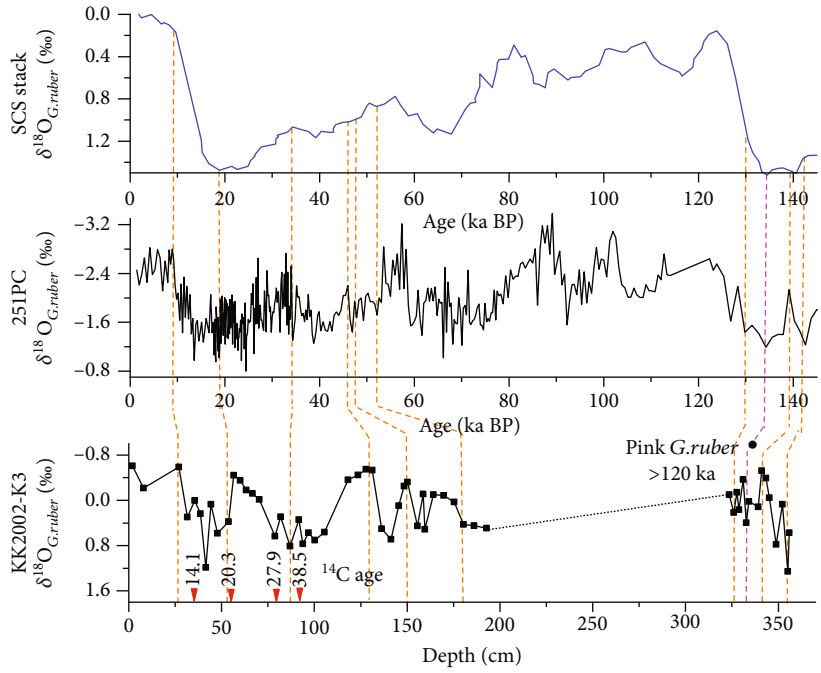

Figure 3: Chronology model for core KK2002-K3. Correlation pattern of $\delta^{18}O$ curves between core KK2002-K3, core 251PC [40], and the South China Sea (SCS) stack [41]. Orange lines represent the planktic foraminiferal $\delta^{18}O$ tie points. The pink line indicates the last occurrence of pink *G. ruber*. Red arrows with numbers indicate the AMS ^{14}C age (cal. ka BP).

Table 1: Radiocarbon dates from core KK2002-K3.

Sample ID	Depth (cm)	Materials	Conventional AMS^{14}C age (a BP)	Cal. ages (a BP)
GZ9804	35.0	Planktonic foraminifera	12645 ± 45	14106.5 ± 110.5
GZ9805	55.0	Planktonic foraminifera	17570 ± 80	20316.5 ± 138.5
GZ10062	78.4	Planktonic foraminifera	24690 ± 200	27992 ± 242
GZ10061	91.3	Planktonic foraminifera	34460 ± 670	38489.5 ± 798.5

diffraction particle analyzer. The analyzer can measure a size range between 0.01 and 3500 μm with a relative error of <2%. The measurements were conducted at the Key Laboratory of Guangdong Higher Education Institute of Climate, Resources and Environment on the Shelf and in the Deep Sea, Guangdong Ocean University. We used the graphical formulation to obtain the grain size parameters [37]. These parameters include mean size (Mz), median size (Md), skewness (Sk), kurtosis (Kg), and sorting coefficient (σi). Mz is typically used to assess total grain size. Sk and Kg, respectively, reflect the asymmetry and pattern of the grain size probability distribution. σi is used to express the degree of grain size uniformity.

3.4. Alkenone-Derived SST. 135 samples of KK2002-K3 were used for alkenone analysis using the method by Kong et al. [38]. The $U^{K'}_{37} = C37:2/(C37:2 + C37:3)$, where C37:2 and C37:3 are the contents of the di- and tri-unsaturated C37 alkenones, respectively. SST was calculated using the calibration equation: $U^{K'}_{37} = 0.031SST + 0.092$ [39]. Standard replication injections in various batches reveal analytical errors for the computed SST less than 0.3°C.

4. Results

4.1. Age Model. The age model of core KK2002-K3 was developed based on AMS ^{14}C ages and planktonic foraminifera $\delta^{18}O$ stratigraphic curves (Figure 3). The calibrated AMS ^{14}C ages at 35 cm, 55 cm, 78 cm, and 91 cm are 14.1, 20.3, 27.9, and 38.5 ka BP, respectively, which were used as age-control points (Table 1). The foraminifera $\delta^{18}O$ curve was compared with the neighbor site 251PC [40] and the planktonic foraminifera $\delta^{18}O_{stack}$ from the SCS [41] (Figure 3). The stratigraphic correlation shows similar glacial-interglacial cycles in the three $\delta^{18}O$ curves [41]. From the correlation, a total of seven $\delta^{18}O$ age-control points in core KK2002-K3 were identified, which agree with the AMS ^{14}C ages. Linear interpolation and extrapolation of four age points associated with the AMS ^{14}C data were performed to develop an age model for core K2002-K3 (Figure 2). The age-tuning results indicate that core KK2002-K3 has a continuous sequence of 142 ka with an average sedimentation rate of approximately 2.5 cm/ka.

4.2. Sediment Property Description. The sediment of core K3 is mainly clayey silt with multiple layers of visible

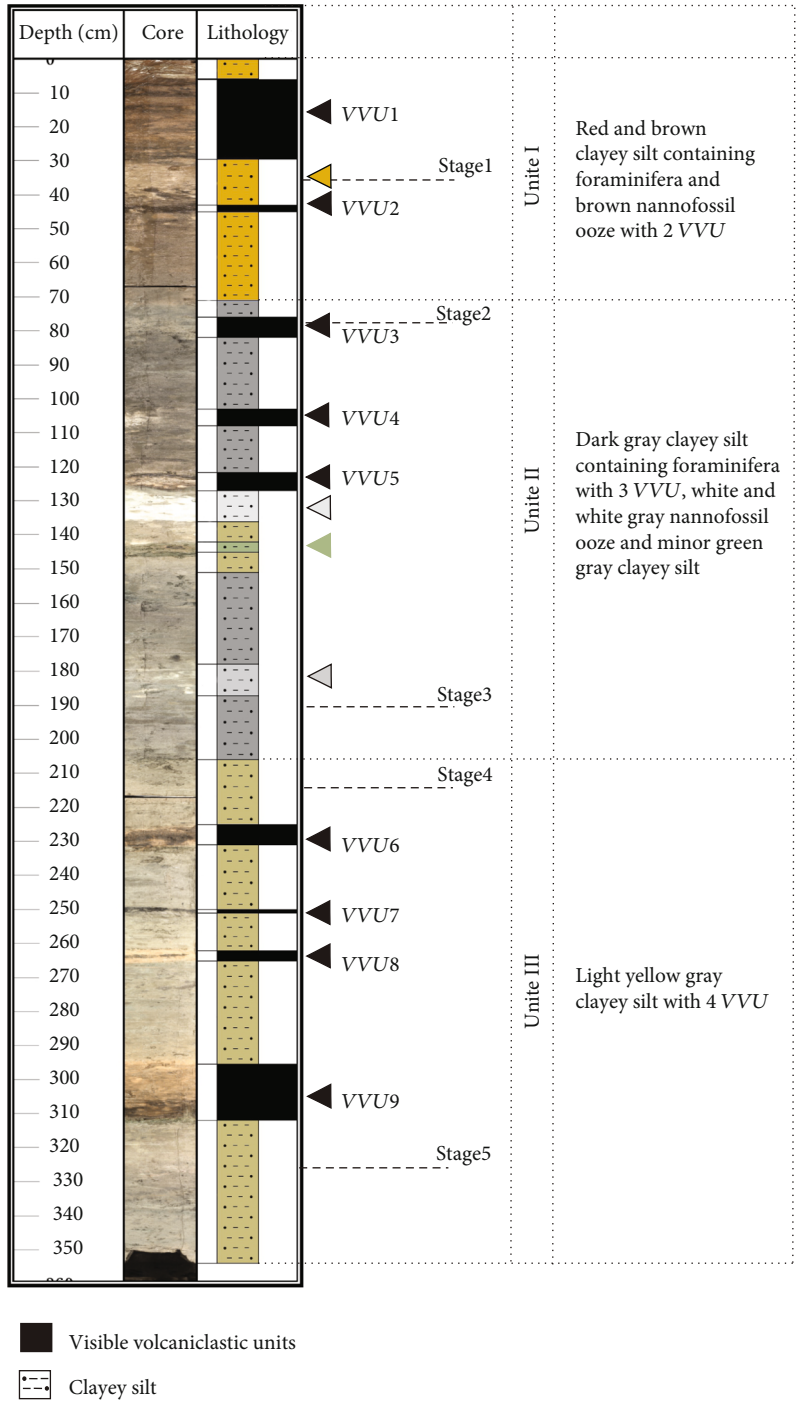

Figure 4: Stratigraphy of core KK2002-K3. Depth in cm is the depth below the seafloor.

volcaniclastic units (VVU 1-9) (Figure 4). It can be roughly divided into three lithological units as follows:

Unit I is 73 cm thick and characterized by red-brown clayey silt. Compared to other units, this unit consists of a greater number of ash layers. The layer observed between 31 and 41 cm is soft fossiliferous clay, containing much planktonic and benthic foraminifera. A probable ash layer was identified throughout unit I at 5-30 cm (VVU 1) and 43-45 cm (VVU 2) (Figure 4), accounting for approximately 33% of the total tephra layer in the unit. VVU 1 and VVU 2 show a sharp basal contact in the sediment. VVU 1 mainly consists of quartz, with some hornblende, mica, magnetite, and biogenic silica, such as foraminifera, diatoms, and radiolarians (Figure S1). Notably, the VVU 2 (43 cm) revealed a large number of ash particles attached to diatoms and radiolarians (Figure S1).

Unit II consists of dark gray clayey silt from 73 to 206 cm. The 77-83 cm (VVU 3) and 104-108 cm (VVU 4) layers in this unit also contain ash layers. They are yellow-brown and mainly composed of hornblende, mica, magnetite,

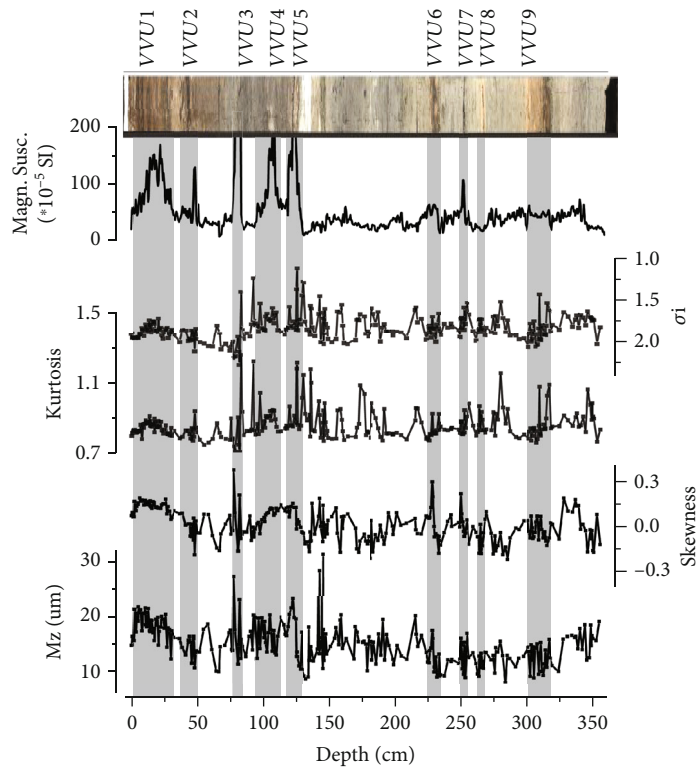

FIGURE 5: Sedimentological log of the core (above), with visible volcaniclastic units highlighted and extrapolated in gray. Magnetic susceptibility and grain size parameter data are plotted for comparison. Depth in cm is the depth below the seafloor.

quartz, and colored volcanic glass and interspersed with visible foraminifera (Figure S1) [42]. The VVU 5 layer has a clear basal contact with many visible black particles. This layer mainly consists of volcanic glass, hornblende, magnetite, and quartz (Figure S1). An 8 cm thick clay-like ultramafic fossiliferous chondrite (128-136 cm) contains a large number of well-preserved radiolarians and diatom shells. The ultramafic clay-like chondrite is mixed with the matrix at 180-188 cm (Figure 4). The lithology in the depths of 143.5-147 cm is dominated by greenish gray clayey silt.

Unit III consists of light yellow-gray clayey silt with a thickness of 206-357 cm. It has four VVUs at 226-232 cm, 251-253 cm, 264-268 cm, and 299-317 cm (Figure 4). Apart from VVU 9, the other three VVUs have sharp basal contacts with adjacent layers. These VVUs are composed of yellowish chalk with a black layer. They contain substantial volcanic glass and pyroclastic grains with biogenic siliceous shells containing bubbles or pores (Figure S1). In VVU 7, a pure black powder volcanic clastic layer and a large number of magnetite and colored volcanic glass have been identified under a microscope. The lithologies of VVU 8 and VVU 9 are the same as those of VVU 6, which include well-preserved biogenic siliceous shells and distinct upper and lower contacts (Figure S1).

4.3. Grain Size Distribution. The mean grain sizes (Mz) of K3 sediments range from 7 to 31 μm. The σi ranges from 1.1 to 2.3 (Figure 5), suggesting that the sediments were poorly sorted [37, 43]. The Kg ranges from 0.7 to 1.3, indicating deposition under a stable hydrodynamic environment [37]. The grain size curves show a clear bimodal distribution, and the median grain sizes of the bimodal peaks range roughly from 4 to 7 μm and 27 to 76 μm (Figure S2). The grain size distribution is similar to those of cores from the eastern SCS [17]. But the grain size distribution curve of core K3 has a small peak at 0.63 μm, which might have resulted from the transportation of fine particulate matter (~0.63 μm) into the SCS basin as stable terrestrial inputs by the westerlies [44].

Generally, all the VVU layers have higher Mz, Sk, Ku, and lower σi than other layers, indicating that the VVUs have greater grain size and better sorting (Figure 5). The grain size distribution of VVUs is obviously characterized by single peak (Figure S2) [17]. The VVUs can be divided into two categories based on their grain size distributions. The first category is the VVUs with only single-peaked grain size distribution (VVU 3, VVU 5, VVU 7, and VVU 9), indicating they were from the rapid deposition of one volcanic eruption. The other VVU category is characterized by bimodal grain size distribution (VVU 1, VVU 2, VVU 4, VVU 6, and VVU 8), which indicates that they might be sourced from both volcanic eruptions and normal sediments.

4.4. Magnetic Susceptibility and XRF Elements. The magnetic susceptibility (MS) of most part of K3 is less than 50×10^{-5} SI. The top part, 0.5-30 cm, has a higher MS reaching 160×10^{-5} SI. Other layers in the depths of 76-85 cm, 100-111 cm, and 118-127 cm show significantly higher MS up

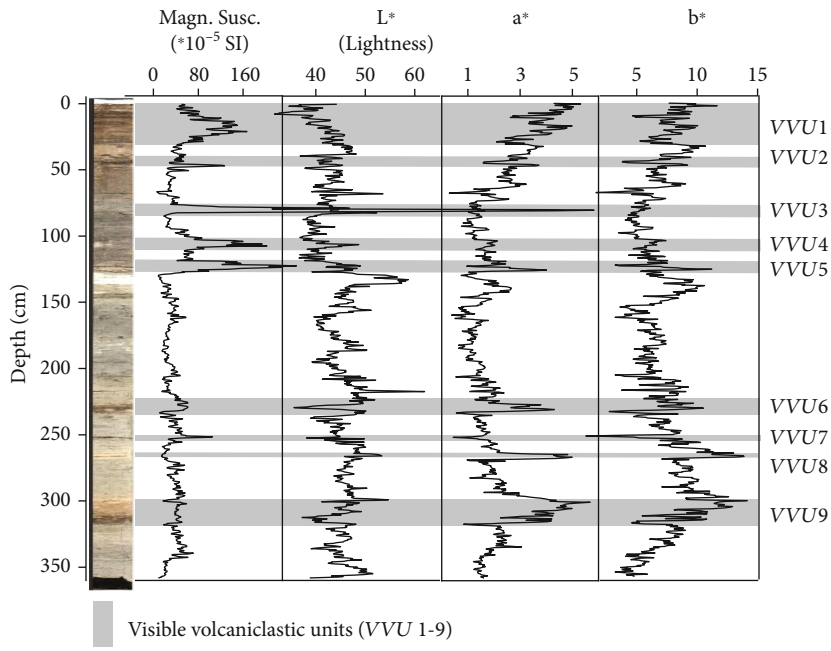

Figure 6: Sedimentological log of the core (left), with visible volcaniclastic units highlighted and extrapolated in gray. Magnetic susceptibility and color spectrophotometry data are plotted for comparison. Depth in cm is the depth below the seafloor.

to 768×10^{-5} SI. Most VVU layers correspond to higher MS (except for VVU 8).

The photometric L* curves differ slightly from a* and b* (Figure 6), which are much more variable. The lower values in L* correspond to 7 of the 9 VVUs (except for VVU 3 and VVU 8). However, the tops or bottoms of volcanic clastic layers are indistinguishable due to interference caused by background signals (e.g., VVU 1). The tephra layers exhibit a wide range of color and brightness properties, most likely attributed to the composition of volcanic eruption materials. The color reflectance data of the core may not serve as the sole indicator for dispersed volcaniclastic sediments, whereas it can be more easily interpreted when combined with magnetic susceptibility [18].

The elemental concentrations of Mn, Fe, K, Zn, Al, Zr, Ca, Sr, and Si in all the VVUs suggest that Mn, Fe, K, Zr, and Si are useful proxies for volcanic detrital materials (Figure S3). In particular, the high concentrations of Fe or Mn, which correspond closely with the presence of VVUs, suggest that these elements may serve as good indicators of tephra occurrences. These elements tend to appear in rock-forming minerals (feldspar, pyroxene, hornblende, and magnetite) that often occur in volcanic rocks (e.g., volcanic rocks outcropped in the Philippines near the eastern part of the SCS).

5. Discussion

Based on the stratigraphic age framework, significant periodic changes of KK2002-K3 SST exhibit high synchronicity with SSTs from MD972142 [45] and 251PC [40] in the eastern SCS, 17954 [39] in the western SCS, and core 17961 [46] in the southern of SCS, as well as the global sea level variation [47] (Figure 7). This synchronicity indicates that SST changes in the SCS were dominated by the global climate which was closely linked to global ice volume. As an important part of the global climate system, the Asian monsoon may play a crucial role in linking high latitude and the tropical SCS [48]. The synchronicity also suggests that the age framework of KK2002-K3 is reliable at the millennial scale, though age errors might be larger than 1 kyr during periods beyond the radiocarbon dating limit.

5.1. The Deposition Processes of K3 Tephra. Sediment sequences in the deep-sea basins could also be influenced by gravity currents. The C-M diagram, where C represents the grain size that corresponds to 1% of the accumulation curve and M represents the median grain size [49], can help identify the gravity flow layers by recognizing graded suspension and bottom suspension [37, 49]. The C-M points of the K3 sample are clustered in a small area, forming a line parallel to the baseline of uniform suspension (Figure 8). This suggests that the sediments of K3 are most likely far from the baseline of C-M, though they do not appear to be distributed on either side. Furthermore, the study site is 3947 m in depth and in a flat basin area, where gravity current is not common. The core site is separated by the Manila Trench from the Philippine Islands. Tephra from the islands could unlikely cross the deep trench by secondary transportation. Therefore, the grain size features of K3 suggest that the VVUs were unlikely formed by gravitational deposition or secondary transportation and are inferred to be fall deposits.

5.2. Identifying Tephra and Cryptotephra Deposits. The magnetic susceptibility over a threshold in JC18-19 cores from

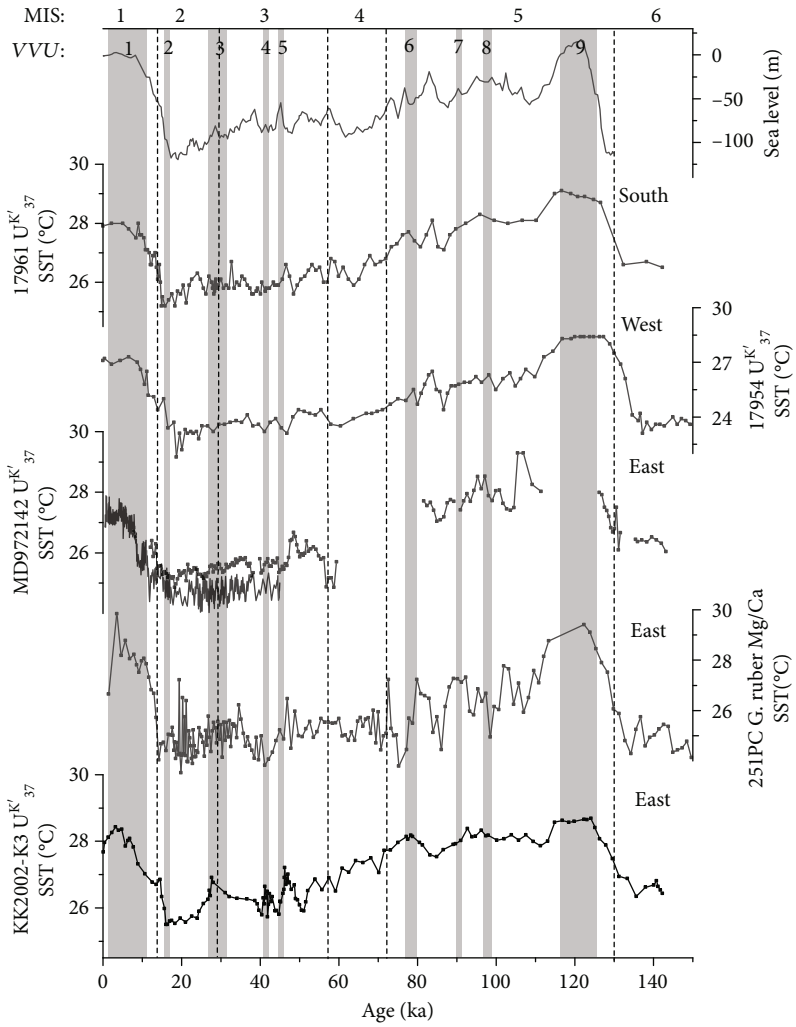

Figure 7: $U^{K'}_{37}$SST records for KK2002-K3, sea level [47], and comparison with other SST records. The eastern of SCS: $U^{K'}_{37}$SST for KK2002-K3 and MD972142 [45] and *G. ruber* Mg/Ca SST for 251PC [40]. The western of SCS: $U^{K'}_{37}$ SST for core 17954 [39] and $U^{K'}_{37}$ SST for core 17961 [46] from the southern SCS. MIS 1–6 and VVU (1–9) are both labeled on the top panel.

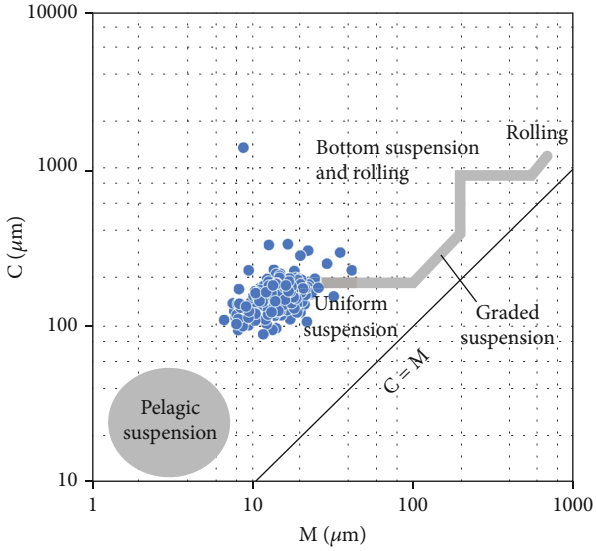

Figure 8: C-M plot of sediments for KK2002-K3 core.

the Montserrat Sea has been proposed as a way to distinguish ash deposits [18]. The threshold setting begins with the visual identification of sections without obvious tephra layers. Then, the MS and element concentrations in these sections were examined to choose the background section with the lowest fluctuation. Values beyond the mean ± 2 standard deviations (2σ) of this background section are considered over the threshold and indicate significant changes (thresholds are shown as orange lines in Figure 9). The lines are the 95 percent (2σ) confidence level (i.e., non-deep-sea material) from the background [50]. Peaks are defined as deviations from the threshold positively or negatively.

After excluding the VVU layers and sections with large fluctuations in element concentration, grain size, and MS, the 278-291 cm was set as the background section (shown as a black block in Figure 9). Its MS threshold ranges from 25.54 to 50.96 ($\times 10^{-5}$ SI). Positive peaks are those above this threshold, and negative peaks are below this threshold. Using this method, eight positive peak levels corresponding

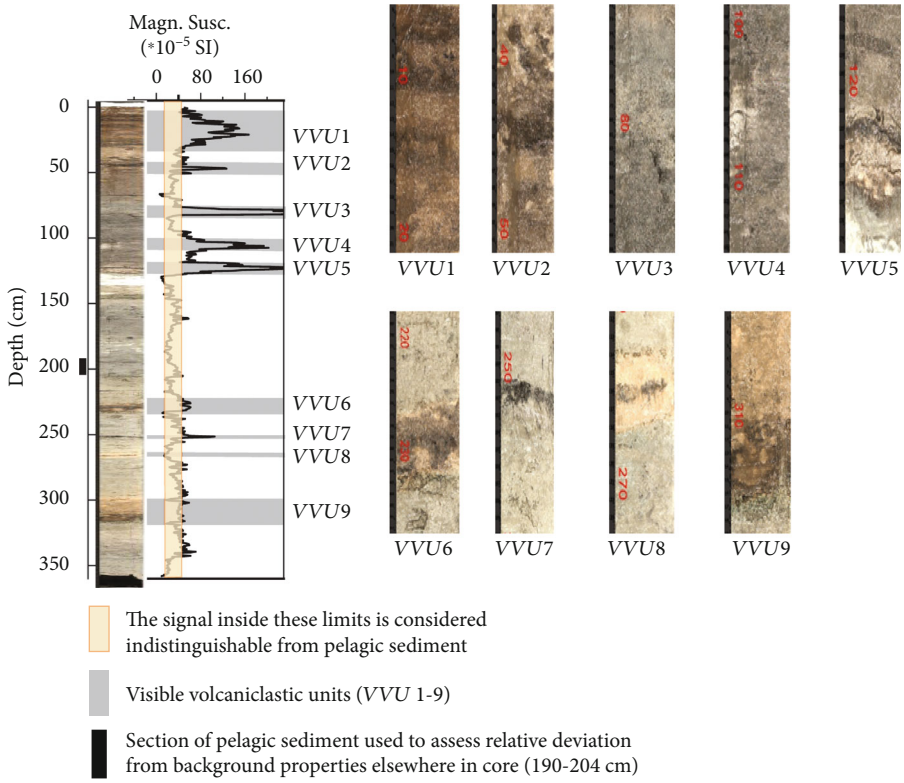

Figure 9: Core photographs of selected marine ash beds (VVU1~9) and KK2002-K3 magnetic susceptibility.

to VVU layers (excluding VVU8) were identified, in agreement with the layers identified by sediment properties.

The MS of sediment is sensitive to changes in ferromagnetic mineral concentration [32, 51, 52], which can be used to identify tephra and igneous rocks [53]. Magnesian-iron volcanic rocks contain high amounts of ferromagnetic minerals (e.g., magnetite, hematite, and titanomagnetite). Basalts, for instance, contain up to 10% iron oxides by weight [51]. As most tephra layers contain a high amount of magnetic minerals, especially magnetite, samples of tephra layers in deep-sea sediments all exhibit anomalous peak MS [15]. However, the VVU 8 has a large number of biogenic silicate shells, which could have diluted magnetic minerals and led to low MS. This is similar to the relatively weak magnetization strengths obtained from the Caribbean Sea [54–56].

Cryptotephras are typically dispersed in deep-sea sediments and composed of glass fragments without strong magnetic signals. The Fe/Ca and Mn/Ca ratios have been successfully applied to identify visible volcanic clastic layers in the Montserrat Sea [18], while cryptotephras are usually determined by a combination of multi-indicator features, such as their negative L^* peaks and positive peaks in MS, Fe/Ca, and Mn/Ca ratios [18]. In the core K3, positive peaks of MS, Fe, and Mn and negative peaks in L^* are used to define the cryptotephras. The threshold range for these parameters is 43.1-48.7 for L^*, 0.85-1.40 for Fe (%), and 0.00-0.07 for Mn (%). If these peaks appear near the VVU layers, they probably have resulted from diagenesis and bioturbation [18] (e.g., between VVU4 and VVU5). After excluding these consecutive peaks, two potential cryptotephras CT_1 and CT_2 could be identified (Figure 10).

Based on the age model, the tephra layers in the core K3 (i.e., VVU 1-9) correspond to ages of 1-11 ka, 16-17 ka, 27-31 ka, 41-42 ka, 45-46 ka, 77-80 ka, 90-91 ka, 97-99 ka, and 116-126 ka. They suggest periods with high eruption frequency or megaeruptions in the eastern part of the SCS. The CT_1 and CT_2 correspond to 49-50 ka and 132-140 ka, respectively. In contrast to the MD972142 volcanic record in the eastern SCS [15], the core K3 recorded more frequent volcanic activities near the Philippine Islands and adjacent areas during 10-13 ka, 26-42 ka, 64-79 ka, and 110-290 ka. Particularly, the VVU6 (77-80 ka) coincides with the tephra layer at 750 cm of MD972142 [15], which was interpreted as a large-scale Toba eruption in Sumatra (~74 ka) [57, 58]. The geochemistry of volcanic glass in VVU 6 will be further investigated to confirm this eruption event. In addition, there are many volcanoes in Indonesia and the Philippines that erupted above VEI 6 during 142 ka (Table 2). The VVU 1 (1-11 ka) overlaps with the 3 Pinatubo (3 ka, 5.5 ka, and 9.4 ka) and Taal (6.8 ka) eruptions in the Philippines. The VVU3 (27-31 ka) possibly agrees with Masurai (3.2 ka) and Ranau (3.3 ka) eruption in Sumatra. CT_1 (49-50 ka) may match the Maninjau eruption (52 ka). The VVU 6 (77-80 ka) not only coincides with the time of the Toba volcano eruption but also with the eruption of the Pinatubo volcano eruption (81 ka). However, these events corresponding to the above volcanic stratigraphy still need further study.

5.3. Implication and Limitation. To carry out further research, the volcanic eruption events can be traced by the geochemical characteristics of volcanic glass [59]. The migration process of volcanic ash can be inferred from

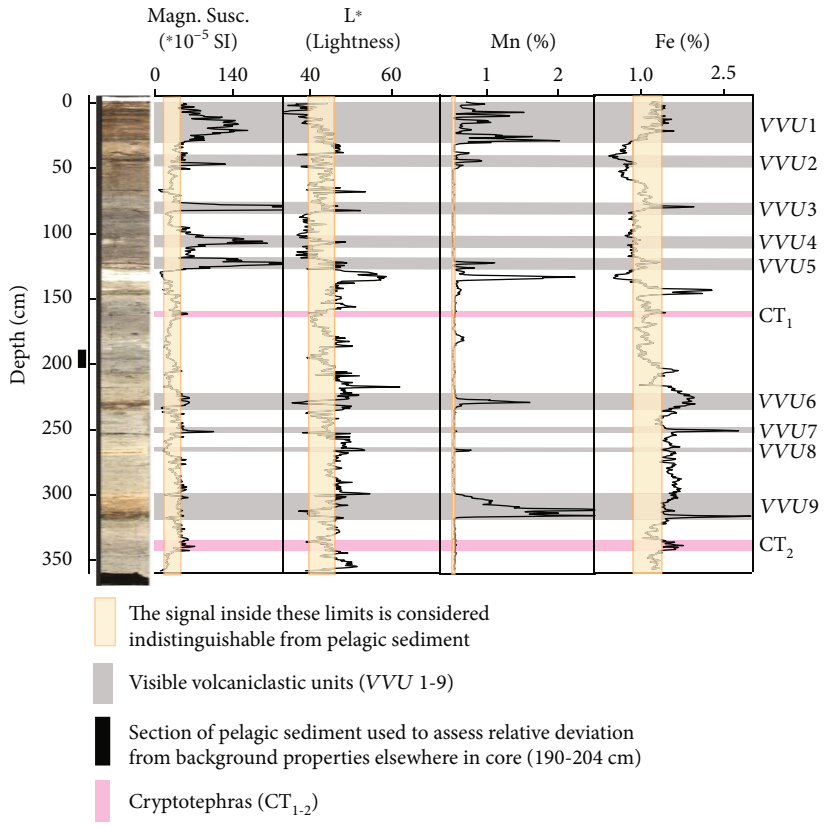

Figure 10: Sedimentological log of the core (left), with visible volcaniclastic units highlighted in gray and cryptotephra units highlighted in pink magnetic susceptibility, and color spectrophotometry data are plotted for comparison. Depth in cm is the depth below the seafloor.

Table 2: The list of dates of VEI 6-8 eruptions in the Philippines and Indonesia over 142 ka. The reported Volcanic Explosivity Index (VEI) is the same for GVP and VOGRIPA. * indicates that we are reporting radiocarbon corrected ages from VOGRIPA. Others are from VOGRIPA (adapted from Caroline et al. [60]).

Source	Region	Eruption name	VEI	Eruption age
Pinatubo	Luzon		6	1991 AD
Krakatau	Sumatra-Java		6	1883 AD
Tambora	Banda		7	1815 AD
Rinjani	Banda	Samalas	7	1257 AD
Pinatubo	Luzon	Maraunot	6	3000 ± 500 cal BP*
Pinatubo	Luzon	Crow Valley	6	5500 ± 500 cal BP*
Taal	Luzon	Taal scoria pyroclastic flow	6	6875 ± 859 BP*
Pinatubo	Luzon	Pasbul	6	9410 ± 150 cal BP*
Batur caldera	Banda	Gunung Kawi ignimbrite	6	24380 ± 3072 cal BP*
Masurai	Sumatra		?	32768 ^{14}C BP
Ranau	Sumatra	Ranau tuff	7	33640 ± 190 cal BP
Batur	Caldera	Bali (or Ubud) ignimbrite	7	34565 ± 3683 cal BP*
Irosin caldera-Bulusan	Caldera	Irosin ignimbrites	6	41329 ± 169 cal BP
Maninjau	Sumatra		7	52 ± 3 ka
Toba	Sumatra	Young Toba tuff	8	73.7 ± 0.3 ka
Pinatubo	Luzon	Inararo Tuff/Tayawan caldera	6	81 ± 2 ka
Tangkuban Parahu	Java	Sunda caldera	6	105 ka

known indicators of particle size parameters [17]. Based on the identification of specific volcanoes, organic biomarkers are used to reconstruct the impact of past volcanic eruptions on climate and marine environment. Though some periods with high volcanic activity are identified, interpreting these signals is still challenging for several reasons. First, the identified layers cannot undoubtedly record the scale of eruptions because the wind direction and the distance from the vent could be quite different during each eruption [17, 18]. Second, as the sedimentation rate in the basin is very low, some tephra layers could be either from a single large eruption or a series of small eruptions (e.g., VVU1).

6. Conclusions

In summary, core KK2002-K3 in the eastern SCS Basin has nine discrete layers of tephra and two layers of cryptotephra, based on sediment properties, grain size, and MS, Fe, and Mn concentrations. Most of them exhibit significant Mn, Fe, and MS peaks and a single peak in grain size distribution. Our studies demonstrated that it is feasible to measure these unique core properties with multisensor core loggers and laser grain size analyzers to trace the presence of tephra. The nine VVU layers and two cryptotephra layers identified from the KK2002-K3 cores are volcanic ash layers rather than gravity deposition. AMS ^{14}C and planktonic foraminiferal $\delta^{18}O$ established depth-age models. The SST changes of KK2002-K3 show good synchronicity with other SST records, suggesting the age model is applicable to a certain extent at the millennial scale. Despite that age errors might be larger than 1 kyr, we still roughly confined volcanic eruptions in the eastern SCS at these intervals: 1-11 ka, 16-17 ka, 27-31 ka, 41-42 ka, 45-46 ka, 49-50 ka, 77-80 ka, 90-91 ka, 97-99 ka, 116-126 ka, and 132-140 ka. This preliminary result provides an opportunity to further investigate the impact of historical eruptions on climate changes and marine/terrestrial environments by involving more biogeochemical approaches.

Data Availability

The data used to support the findings of this study can be accessed by contacting the corresponding author.

Conflicts of Interest

The authors declare that there is no conflict of interest.

Acknowledgments

This work was funded by the National Key Research and Development Program of China (2018YFA0605601), the National Natural Science Foundation of China (41606070), the Program for Scientific Research Start-Up Funds of Guangdong Ocean University (R17011), and the Guangdong Provincial College Innovation Team Project (2019KCXTF021). The sediment core KK2002-K3 was collected onboard of R/V "Tan Kah Kee" implementing the open research cruise NORC2019-06, which was supported by NSFC Shiptime Sharing Project (project number: 41849906).

Supplementary Materials

Supplementary 1. Figure S1: microscope photograph of VVU 1~9. (a) Volcanic glass. (b) Biosilicon. (c) Volcanic slag ash.

Supplementary 2. Figure S2: grain size distributions of the visible volcaniclastic units and sediment background in the eastern South China Sea basin.

Supplementary 3. Figure S3: image of the core (left), with visible volcaniclastic units highlighted and extrapolated in gray. Different element is plotted from the XRF core scanning data. Depth in cm is the depth below the seafloor.

References

[1] C. Oppenheimer, "Volcanic degassing," *Treatise on Geochemistry*, vol. 3, p. 659, 2003.

[2] A. Robock, "Correction to "Volcanic eruptions and climate"," *Reviews of Geophysics*, vol. 45, no. 3, 2007.

[3] C. C. Gao, A. Robock, and C. Ammann, "Correction to "Volcanic forcing of climate over the past 1500 years: an improved ice core-based index for climate models"," *Journal of Geophysical Research-Atmospheres*, vol. 114, no. D9, 2009.

[4] C. Textor, H. F. Graf, M. Herzog, and J. M. Oberhuber, "Injection of gases into the stratosphere by explosive volcanic eruptions," *Journal of Geophysical Research-Atmospheres*, vol. 108, no. D19, pp. 1–17, 2003.

[5] M. P. McCormick, L. W. Thomason, and C. R. Trepte, "Atmospheric effects of the Mt Pinatubo eruption," *Nature*, vol. 373, no. 6513, pp. 399–404, 1995.

[6] Pinatubo Volcano Observatory Team, "Lessons from a major eruption: Mt. Pinatubo, Philippines," *Eos, Transactions American Geophysical Union*, vol. 72, no. 49, pp. 545–555, 1991.

[7] D. Swingedouw, J. Mignot, P. Ortega, M. Khodri, and V. Hanquiez, "Impact of explosive volcanic eruptions on the main climate variability modes," *Global and Planetary Change*, vol. 150, pp. 24–45, 2017.

[8] T. Nakanishi, M. Torii, K. Yamasaki et al., "Tephra identification and radiocarbon chronology of sediment from Paitan Lake at the northern part of Luzon Central Plain, Philippines," *Quaternary International*, vol. 456, no. 15, pp. 210–216, 2017.

[9] S. Wulf, J. Keller, M. Paterne et al., "The 100-133 ka record of Italian explosive volcanism and revised tephrochronology of Lago Grande di Monticchio," *Quaternary Science Reviews*, vol. 58, pp. 104–123, 2012.

[10] S. V. D. Kaars, M. A. J. Williams, F. Bassinot et al., "The influence of the ~73 ka Toba super-eruption on the ecosystems of northern Sumatra as recorded in marine core BAR94-25," *Quaternary International*, vol. 258, pp. 45–53, 2012.

[11] E. R. Gudmundsdóttir, J. Eiríksson, and G. Larsen, "Identification and definition of primary and reworked tephra in Late Glacial and Holocene marine shelf sediments off North Iceland," *Journal of Quaternary Science*, vol. 26, no. 6, pp. 589–602, 2011.

[12] S. Kutterolf, A. Freundt, W. Peréz et al., "Pacific offshore record of plinian arc volcanism in Central America: 1. Along-arc correlations," *Geochemistry Geophysics Geosystems*, vol. 9, no. 2, pp. 1–26, 2008.

[13] J. C. Schindlbeck, M. Jegen, A. Freundt et al., "100- kyr cyclicity in volcanic ash emplacement: evidence from a 1.1 Myr tephra record from the NW Pacific," *Scientific Reports*, vol. 8, no. 1, article 4440, 2018.

[14] Z. B. Shi, X. T. Lin, Q. H. Yang, F. Y. Zhang, and Z. H. Lin, "Volcanic sediments in the eastern South China Sea during the Late Pleistocene epoch (in Chinese with English abstract)," *Journal of Ocean University of Qingdao*, vol. 34, no. 6, pp. 1063–1068, 2004.

[15] K. Wei and T. Lee, "Late Pleistocene volcanic ash layers in core MD972142,offshore from northwestern Palawan, South China Sea: a preliminary report," *Terrestrial Atmospheric & Oceanic Sciences*, vol. 9, no. 1, pp. 143–152, 1998.

[16] M. G. Wiesner, Y. Wang, and L. Zheng, "Fallout of volcanic ash to the deep South China Sea induced by the 1991 eruption of Mount Pinatubo (Philippines)," *Geology*, vol. 23, no. 10, pp. 885–888, 1995.

[17] M. G. Wiesner, A. Wetzel, S. G. Catane, E. L. Listanco, and H. T. Mirabueno, "Grain size, areal thickness distribution and controls on sedimentation of the 1991 Mount Pinatubo tephra layer in the South China Sea," *Bulletin of Volcanology*, vol. 67, no. 3, pp. 490–495, 2005.

[18] M. Cassidy, S. F. L. Wait, M. R. Palmer et al., "Construction of volcanic records from marine sediment cores: a review and case study (Montserrat, West Indies)," *Earth-Science Reviews*, vol. 138, pp. 137–155, 2014.

[19] Z. Liu, Y. Zhao, C. Colin et al., "Source-to-sink transport processes of fluvial sediments in the South China Sea," *Earth-Science Reviews*, vol. 153, pp. 238–273, 2016.

[20] P. L. Whelley, C. G. Newhall, and K. E. Bradley, "The frequency of explosive volcanic eruptions in Southeast Asia," *Bulletin of Volcanology*, vol. 77, no. 1, pp. 1–11, 2015.

[21] H. S. Crosweller, B. Arora, S. K. Brown et al., "Global database on large magnitude explosive volcanic eruptions (LaMEVE)," *Journal of Applied Volcanology*, vol. 1, no. 1, pp. 1–13, 2012.

[22] S. P. E. Blockley, A. J. Bourne, A. Brauer et al., "Tephrochronology and the extended intimate (integration of ice-core, marine and terrestrial records) event stratigraphy 8-128 ka b2k," *Quaternary Science Reviews*, vol. 106, pp. 88–100, 2014.

[23] G. Zanchetta, M. Bini, M. A. Di Vito, R. Sulpizio, and L. Sadori, "Tephrostratigraphy of paleoclimatic archives in Central Mediterranean during the Bronze Age," *Quaternary International*, vol. 499, pp. 186–194, 2019.

[24] R. G. Rothwell and F. R. Rack, "New techniques in sediment core analysis: an introduction," *Geological Society London Special Publications*, vol. 267, no. 1, pp. 1–29, 2006.

[25] M. C. Mccanta, R. G. Hatfield, B. J. Thomson, S. J. Hook, and E. Fisher, "Identifying cryptotephra units using correlated rapid, nondestructive methods: VSWIR spectroscopy, X-ray fluorescence, and magnetic susceptibility," *Geochemistry Geophysics Geosystems*, vol. 16, no. 12, pp. 4029–4056, 2015.

[26] K. Takemura, A. Hayashida, M. Okamura et al., "Stratigraphy of multiple piston-core sediments for the last 30,000 years from Lake Biwa, Japan," *Journal of Paleolimnology*, vol. 23, no. 2, pp. 185–199, 2000.

[27] T. L. Rasmussen, S. Wastegård, A. Kuijpers, T. Weering, J. Heinemeier, and E. Thomsen, "Stratigraphy and distribution of tephra layers in marine sediment cores from the Faeroe Islands, North Atlantic," *Marine Geology*, vol. 199, no. 3-4, pp. 263–277, 2003.

[28] H. Vogel, G. Zanchetta, R. Sulpizio, B. Wagner, and N. Nowaczyk, "A tephrostratigraphic record for the last glacial–interglacial cycle from Lake Ohrid, Albania and Macedonia," *Journal of Quaternary Science*, vol. 25, no. 3, pp. 320–338, 2010.

[29] L. Carter and B. Manighetti, "Glacial/interglacial control of terrigenous and biogenic fluxes in the deep ocean off a high input, collisional margin: a 139 kyr-record from New Zealand," *Marine Geology*, vol. 226, no. 3-4, pp. 307–322, 2006.

[30] L. Kristjansson and G. Jonsson, "Paleomagnetism and magnetic anomalies in Iceland," *Journal of Geodynamics*, vol. 43, no. 1, pp. 30–54, 2007.

[31] M. J. Gehrels, R. M. Newnham, D. J. Lowe, S. Wynne, Z. J. Hazell, and C. J. Caseldine, "Towards rapid assay of cryptotephra in peat cores: review and evaluation of various methods," *Quaternary International*, vol. 178, no. 1, pp. 68–84, 2008.

[32] J. A. Dearing, "Environmental magnetic susceptibility," *Using the Bartington MS2 System*, vol. 32, 1999.

[33] J. Brendryen, H. Haflidason, and H. P. Sejrup, "Norwegian Sea tephrostratigraphy of marine isotope stages 4 and 5: prospects and problems for tephrochronology in the North Atlantic region," *Quaternary Science Reviews*, vol. 29, no. 7-8, pp. 847–864, 2010.

[34] M. E. Kylander, E. M. Lind, S. Wastegard, and L. Lowemark, "Recommendations for using XRF core scanning as a tool in tephrochronology," *Holocene*, vol. 22, no. 3, pp. 371–375, 2012.

[35] A. J. Nederbragt, R. B. Dunbar, A. T. Osborn, A. Palmer, and T. Wagner, "Sediment colour analysis from digital images and correlation with sediment composition," *Geological Society of London*, vol. 267, no. 1, pp. 113–128, 2006.

[36] C. Caseldine, A. Baker, and W. L. Barnes, "A rapid, non-destructive scanning method for detecting distal tephra layers in peats," *Holocene*, vol. 9, no. 5, pp. 635–638, 1999.

[37] R. Passega, "Texture as characteristic of clastic deposition," *AAPG Bulletin*, vol. 41, pp. 1952–1984, 1957.

[38] D. Kong, Y. Zong, G. Jia, G. Wei, M. T. Chen, and Z. Liu, "The development of late Holocene coastal cooling in the northern South China Sea," *Quaternary International*, vol. 349, pp. 300–307, 2014.

[39] C. Pelejero and J. O. Grimalt, "The correlation between the $_{37}^{k}$ index and sea surface temperatures in the warm boundary: the South China Sea," *Geochimica et Cosmochimica Acta*, vol. 61, no. 22, pp. 4789–4797, 1997.

[40] Q. Zhou, J. Yin, X. Yang, Q. Chen, Y. Xie, and H. Zhang, "Planktic foraminiferal $\delta^{18}O$ values indicate precipitation variability in the southeastern South China Sea over the last 175 ka BP," *Quaternary Science Reviews*, vol. 253, no. 1, article 106745, 2021.

[41] P. Wang, Q. Li, J. Tian et al., "Monsoon influence on planktic $\delta^{18}O$ records from the South China Sea," *Quaternary Science Reviews*, vol. 142, pp. 26–39, 2016.

[42] K. Ikehara, "Marine tephra in the Japan Sea sediments as a tool for paleoceanography and paleoclimatology," *Progress in Earth and Planetary Science*, vol. 2, no. 1, p. 36, 2015.

[43] T. Ito, Y. Komatsu, T. Fujii et al., "Lithological features of hydrate-bearing sediments and their relationship with gas hydrate saturation in the eastern Nankai Trough, Japan," *Marine and Petroleum Geology*, vol. 66, pp. 368–378, 2015.

[44] S. Du, R. Xiang, J. Liu, J. P. Liu, G. M. A. Islam, and M. Chen, "The present-day atmospheric dust deposition process in the

South China Sea," *Atmospheric Environment*, vol. 223, no. 15, article 117261, 2020.

[45] D. Li, M. Zhao, and M. T. Chen, "Corrigendum to: "East Asian winter monsoon controlling phytoplankton productivity and community structure changes in the southeastern South China Sea over the last 185 kyr" [Palaeo 414C (2014) 233-242]," *Palaeogeography Palaeoclimatology Palaeoecology*, vol. 417, pp. 576–576, 2015.

[46] C. Pelejero, J. O. Grimalt, S. Heilig, M. Kienast, and L. Wang, "High-resolution $U^{k'}_{37}$ temperature reconstructions in the South China Sea over the past 220 kyr," *Paleoceanography and Paleoclimatology*, vol. 14, no. 2, pp. 224–231, 1999.

[47] M. Siddall, E. J. Rohling, A. Almogi-Labin et al., "Sea-level fluctuations during the last glacial cycle," *Nature*, vol. 423, no. 6942, pp. 853–858, 2003.

[48] M. Zhao, C. Y. Huang, C. C. Wang, and G. Wei, "A millennial-scale $U_{37}^{K'}$ sea-surface temperature record from the South China Sea (8°N) over the last 150 kyr: monsoon and sea-level influence," *Palaeogeography, Palaeoclimatology, Palaeoecology*, vol. 236, no. 1-2, pp. 39–55, 2006.

[49] R. Passega, "Grain size representation by CM patterns as a geologic tool," *Journal of Sedimentary Research*, vol. 34, no. 4, pp. 830–847, 1964.

[50] A. L. Currie, "Limits for qualitative detection and quantitative determination. Application to radiochemistry," *Analytical Chemistry*, vol. 40, no. 3, pp. 586–593, 1968.

[51] R. Thompson and F. Oldfield, "Environmental magnetism," *Open Journal of Geology*, vol. 8, no. 4, 1986.

[52] E. M. Evans and F. Heller, "Environmental magnetism: principles and applications of enviromagnetics," *Eos, Transactions American Geophysical Union*, vol. 85, no. 20, pp. 202–202, 2004.

[53] C. F. Li, J. Lin, and D. K. Kulhanek, *Proceedings of the International Ocean Discovery Program*, South China Sea Tectonics, 2015, http://iodp.org.

[54] R. Pamela Reid and C. R. Ross, "Late Quaternary sedimentation in the Lesser Antilles island arc," *GSA Bulletin*, vol. 108, no. 1, pp. 78–100, 1996.

[55] D. Wallpalmer, M. B. Hart, C. W. Smart et al., "Pteropods from the Caribbean Sea: variations in calcification as an indicator of past ocean carbonate saturation," *Biogeosciences*, vol. 9, no. 1, pp. 309–315, 2012.

[56] D. Wall-Palmer, M. Coussens, P. J. Talling et al., "Late Pleistocene stratigraphy of IODP site U1396 and compiled chronology offshore of south and south west Montserrat, Lesser Antilles," *Geochemistry, Geophysics, Geosystems*, vol. 15, no. 7, pp. 3000–3020, 2014.

[57] J. A. Westgate, N. J. G. Pearce, W. T. Perkins, S. J. Preece, C. A. Chesner, and R. F. Muhammad, "Tephrochronology of the Toba tuffs: four primary glass populations define the 75-ka Youngest Toba Tuff, northern Sumatra, Indonesia," *Journal of Quaternary Science*, vol. 28, no. 8, pp. 772–776, 2013.

[58] N. J. G. Pearce, J. A. Westgate, E. Gatti, J. N. Pattan, G. Parthiban, and H. Achyuthan, "Individual glass shard trace element analyses confirm that all known Toba tephra reported from India is from the c. 75-ka Youngest Toba eruption," *Journal of Quaternary Science*, vol. 29, no. 8, pp. 729–734, 2014.

[59] D. J. Lowe, N. J. G. Pearce, M. A. Jorgensen, S. C. Kuehn, C. A. Tryon, and C. L. Hayward, "Correlating tephras and cryptotephras using glass compositional analyses and numerical and statistical methods: review and evaluation," *Quaternary Science Reviews*, vol. 175, pp. 1–44, 2017.

[60] B. Caroline, D. Maisonneuve, and O. Bergal-Kuvikas, "Timing, magnitude and geochemistry of major southeast Asian volcanic eruptions: identifying tephrochronologic markers," *Journal of Quaternary Science*, vol. 35, no. 1-2, pp. 272–287, 2020.